SCIENTIFIC REPORTS

OPEN

Fe-Sn nanocrystalline films for flexible magnetic sensors with high thermal stability

Y. Satake[1], K. Fujiwara[1], J. Shiogai[1], T. Seki[1,2] & A. Tsukazaki [1,2]

The interplay of magnetism and spin-orbit coupling on an Fe kagome lattice in Fe_3Sn_2 crystal produces a unique band structure leading to an order of magnitude larger anomalous Hall effect than in conventional ferromagnetic metals. In this work, we demonstrate that Fe-Sn nanocrystalline films also exhibit a large anomalous Hall effect, being applicable to magnetic sensors that satisfy both high sensitivity and thermal stability. In the films prepared by a co-sputtering technique at room temperature, the partial development of crystalline lattice order appears as nanocrystals of the Fe-Sn kagome layer. The tangent of Hall angle, the ratio of Hall resistivity to longitudinal resistivity, is maximized in the optimal alloy composition of close to Fe_3Sn_2, implying the possible contribution of the kagome origin even though the films are composed of nanocrystal and amorphous-like domains. These ferromagnetic Fe-Sn films possess great advantages as a Hall sensor over semiconductors in thermal stability owing to the weak temperature dependence of the anomalous Hall responses. Moreover, the room-temperature fabrication enables us to develop a mechanically flexible Hall sensor on an organic substrate. These demonstrations manifest the potential of ferromagnetic kagome metals as untapped reservoir for designing new functional devices.

Iron-based alloys and compounds have constituted the outstanding basis for applications, particularly with judicious utilization of their rich magnetism and magneto-transport characteristics[1–4]. To enrich their functionality further, extensive investigations have continued on iron-based ferromagnetic materials including ordered alloys[5], oxides[6], and nitrides[7]. In this study, we exemplify magnetic sensor functions in a ferromagnetic iron-tin alloy that is fabricated to harness massive Dirac bands of the kagome metal Fe_3Sn_2 (ref.[8]). Magnetic sensors are capable of electrically detecting a magnetic field[9] and are becoming increasingly important towards the acceleration of Internet of Things. Their applications include monitoring of electric current via the Oersted field, electronic compasses and motion detection of mechanical parts in microdevices. In conventional semiconductor Hall sensors, the detection of a magnetic field B (termed instead of magnetic induction, hereafter) relies on the ordinary Hall effect, which converts a flow of electric current to the transverse Hall voltage V_{yx} (ref.[10]). Since the output V_{yx} is proportional to B and the injection current, good sensor performance under a constant input voltage is achieved in III–V semiconductors such as GaAs, InAs, and InSb with a high carrier mobility[10]. These semiconductor devices are constructed essentially on highly crystalline films with a low carrier density precisely tuned by high-temperature growth. Their bandgaps are, however, inevitably accompanied by substantial temperature (T) dependences of device characteristics. To ensure the stable operation in a wide T range, an external circuit that compensates the T dependence needs to be implemented.

Without changing the basic device structure, the semiconductor can be replaced by a ferromagnetic material if the anomalous Hall effect (AHE) is sufficiently large and provides a linear response to the applied B. V_{yx} induced by AHE is a nominal function of magnetization M and is proportional to tangent of Hall angle, the ratio of Hall resistivity to longitudinal resistivity; materials design is thus better guided with tangent of Hall angle rather than mobility and carrier density. However, conventional ferromagnetic metals such as Fe, Co, and Ni show low tangent of Hall angle values of less than approximately 0.01 (ref.[11]), and are not suited to AHE-type Hall sensors. In the past two decades, significant progress has been made in the development of AHE materials and understanding of their physical origins[11]. Of particular interest is the intrinsic AHE where Berry curvature arising from electronic band topology acts as an effective magnetic field and can produce a large tangent of Hall angle and V_{yx}.

[1]Institute for Materials Research, Tohoku University, Sendai, 980-8577, Japan. [2]Center for Spintronics Research Network (CSRN), Tohoku University, Sendai, 980-8577, Japan. Correspondence and requests for materials should be addressed to K.F. (email: kfujiwara@imr.tohoku.ac.jp)
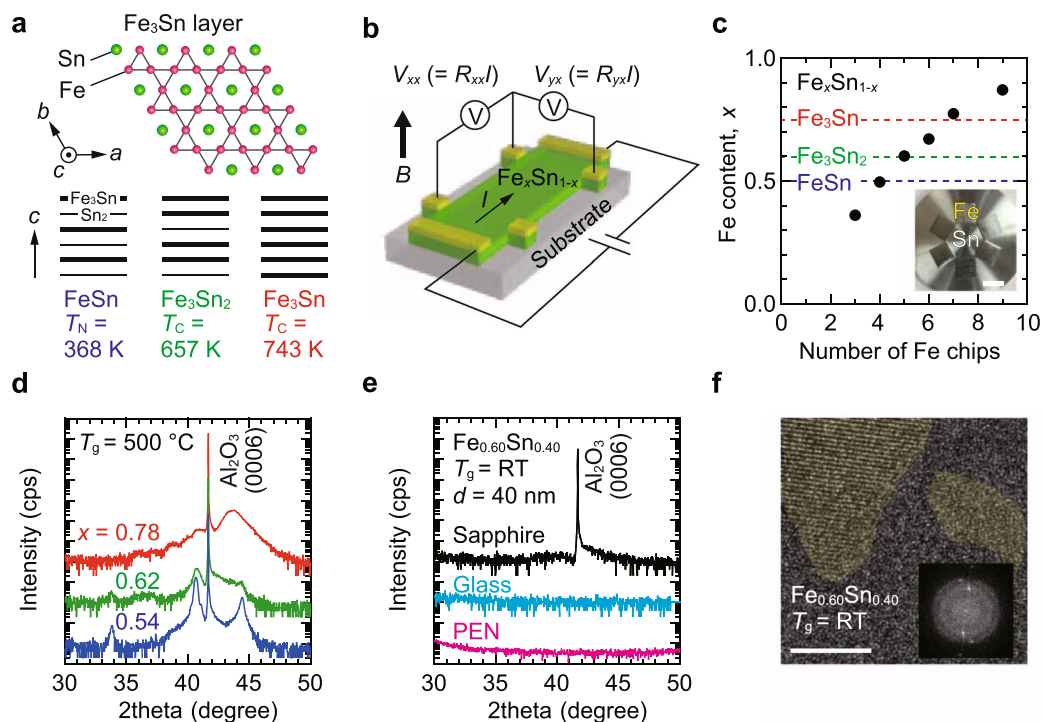
Figure 1. Sputtered Fe-Sn alloy films. (**a**) Layered Fe-Sn kagome compounds. The Fe_3Sn kagome layer is depicted in the upper side, and the layer stackings in antiferromagnetic FeSn, ferromagnetic Fe_3Sn_2 and Fe_3Sn are displayed in the lower side. (**b**) The device structure is shown schematically. An excitation current I was injected to an Fe-Sn film on an insulating substrate, and longitudinal voltage V_{xx} and transverse Hal voltage V_{yx} were measured. A magnetic field B is applied perpendicularly to the film plane. (**c**) Fe content x in Fe_xSn_{1-x} films was controlled by changing the Fe chip configuration on the Sn target. Error bars (standard deviations for x) are smaller than the symbols. A photograph when six Fe chips are placed is shown in the inset. The scale bar shows 10 mm. Blue, green, and, red broken lines correspond to $x = 0.50$ (FeSn), 0.60 (Fe_3Sn_2), and 0.75 (Fe_3Sn), respectively. (**d**) XRD patterns for Fe_xSn_{1-x} films with $x = 0.54$, 0.62, and 0.78 grown on sapphire (0001) substrates at $T_g = 500\,°C$. The data are shifted vertically for clarity. The film thicknesses were approximately 40 nm. See the text and Supplementary Fig. S1 for the phase identification of these films. (**e**) XRD patterns for 40-nm-thick $Fe_{0.60}Sn_{0.40}$ films on sapphire, glass and, PEN sheet substrates prepared at room temperature. (**f**) (False color image) Cross-sectional high-resolution transmission electron microscopy image of a room-temperature sputtered $Fe_{0.60}Sn_{0.40}$ film on a sapphire substrate. The scale bar shows 5 nm. The inset shows a selected area electron diffraction pattern, revealing the presence of nanocrystalline domains.

In this context, a ferromagnetic Fe-Sn compound, Fe_3Sn_2 (Curie temperature $T_C = 657\,K$), is attracting attention because of its very large AHE at room temperature[8,12,13]. The crystal structure consists of alternate stacking of stanene and a bilayer of Fe_3Sn with a kagome network of Fe, as illustrated in Fig. 1a. A recent angle-resolved photoemission spectroscopic study proposed that an interplay of the kagome lattice, which in analogy to graphene produces linearly dispersed bands and Dirac points, and spin-orbit coupling yields massive Dirac bands that concentrate Berry curvature[8]. By positioning the Fermi level within the gap, e.g. with electrostatic gating and impurity doping, quantized AHE[14,15] may be realized at room temperature. Fe_3Sn_2 is, however, the high-temperature phase stable above 607 °C; the bulk crystal is formed by a quenching technique[8,12,13,16,17]. Recognizing the uniqueness of Fe_3Sn_2, we focus on the thin film of Fe-Sn kagome compounds[18,19] as a candidate for AHE-type Hall sensors (Fig. 1b). Here we demonstrate magnetic sensor functions of nanocrystalline Fe-Sn alloy films prepared by room-temperature sputtering. Despite the lack of macroscopic lattice order, these films clearly bear characteristics of the crystalline Fe-Sn phase diagram and exhibit large and linear AHE responses as in the Fe_3Sn_2 bulk. This metal-based Hall device can outperform conventional semiconductor Hall sensors in thermal stability. The integration on a bendable polymer sheet thanks to the room-temperature fabrication is demonstrated for potential use in flexible electronics. These findings should accelerate challenges to exploitation of exotic physics hosted by iron and other transition-metal kagome compounds[20–23].

Results

Fe-Sn nanocrystalline films grown by co-sputtering at room temperature.
Fe_xSn_{1-x} alloy films were fabricated by a co-sputtering technique[18,19]. The two elements were supplied from a single magnetron cathode by mounting Fe chips on a Sn target (Fig. 1c inset and also see Methods section). In the Fe-Sn binary members[16], antiferromagnetic FeSn (Néel temperature $T_N = 368\,K$) and ferromagnetic Fe_3Sn ($T_C = 743\,K$, refs[24,25]) also exist, in which the Fe_3Sn kagome layers are accommodated with different stacking sequences (Fig. 1a). To cover these kagome
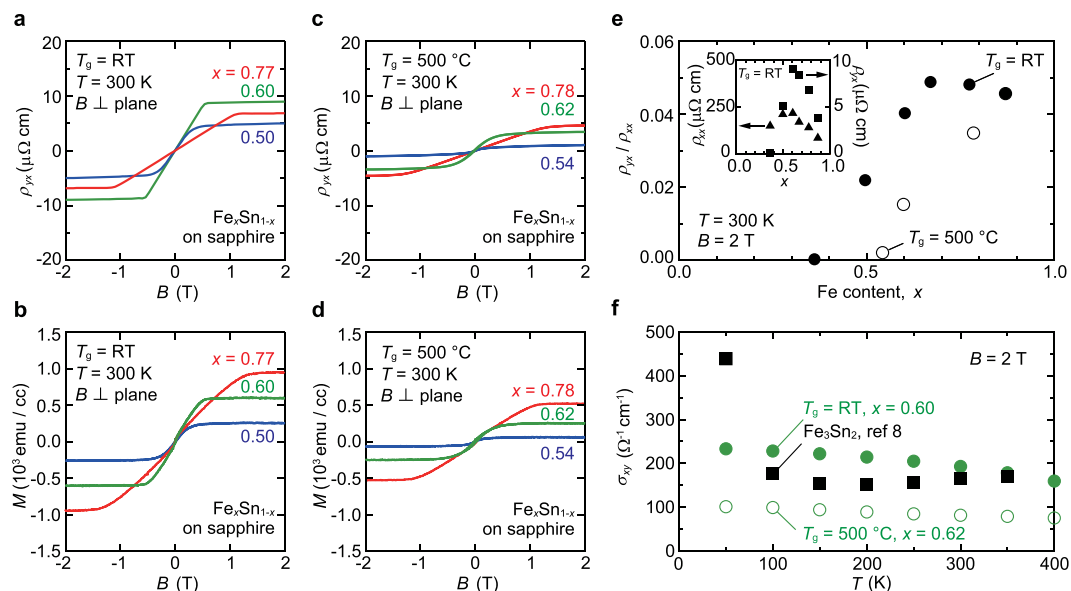
Figure 2. AHE in nanocrystalline Fe-Sn alloy films. (**a**,**b**) Hall resistivity ρ_{yx} (**a**) and out-of-plane magnetization M (**b**) at $T = 300\,\text{K}$ measured for room-temperature sputtered nanocrystalline Fe_xSn_{1-x} films as a function of an out-of-plane magnetic field B. The film magnetization was extracted by subtracting diamagnetic contributions from the data measured. (**c**,**d**) The results for polycrystalline Fe_xSn_{1-x} films grown at $T_g = 500\,°\text{C}$. (**e**) x dependence of tangent of Hall angle, ρ_{yx}/ρ_{xx}, at $B = 2\,\text{T}$ and $T = 300\,\text{K}$ for nanocrystalline (filled black circles) and polycrystalline Fe_xSn_{1-x} films (open black circles). The inset shows ρ_{xx} (triangles) and ρ_{yx} (squares) for nanocrystalline Fe_xSn_{1-x}. (**f**) T dependence of Hall conductivity σ_{xy} for a nanocrystalline $Fe_{0.60}Sn_{0.40}$ film (filled green circles) and a polycrystalline $Fe_{0.62}Sn_{0.38}$ film (open green circles). For reference, the data of Fe_3Sn_2 bulk in literature (ref.[8]) are also included (filled black squares).

compounds widely, the Fe content x in the films was varied by the Fe chip number as displayed in Fig. 1c. The in-plane distribution of x was as small as a few atomic percent. Figure 1d shows X-ray diffraction (XRD) patterns of films with various x, grown on single-crystalline sapphire (0001) substrates at a growth temperature T_g of $500\,°\text{C}$. Nearly equimolar mixture of Fe and Sn ($x = 0.54$) yields a single phase of FeSn (see Fig. S1 in the Supplementary Information for peak identification). For $x = 0.62$, diffuse reflections of Fe_3Sn_2 are recognized though FeSn still remains. For $x = 0.78$, the Fe_3Sn phase grows in addition to FeSn. Of the three kagome metals, FeSn is thermodynamically stable and the other two are easily decomposed into FeSn and Sn-rich α-Fe on cooling after high-temperature crystallization[16]; the above XRD results are consistent with the bulk behavior. As shown in Fig. 1e, the formation of FeSn is found to be suppressed by room-temperature sputtering. Also, macroscopically, the room-temperature grown films do not have crystalline character. Cross-sectional transmission electron microscopy, however, reveals the presence of nanocrystalline domains with typical sizes of as small as a few nanometers, as displayed in Fig. 1f (scale bar, 5 nm). Although d-spacing values calculated from the selected-area electron diffraction pattern (Fig. 1f inset) are not uniquely indexed with one of the three compounds, the clearly visible layered lattice, together with the detailed characterization (Fig. S2 in the Supplementary Information), suggests the existence of Fe_3Sn_2-like domains in the nanocrystalline film with $x = 0.60$. Considering that further characterization is required for the comprehensive phase analysis, we hereafter focus on composition dependent AHE characteristics in these mixed-phase films rather than quantifying physical properties of each phase.

Comparison of anomalous Hall responses in nanocrystalline and polycrystalline films.

Contrary to a naive expectation that the large AHE driven by band topology of the kagome lattice should smear out in such nanocrystalline films, we observed a clear AHE in the room-temperature grown nanocrystalline Fe_xSn_{1-x}. Figure 2a,b show Hall resistivity ρ_{yx} and magnetization M plots, respectively, measured at 300 K under the out-of-plane B application. It is obvious that ρ_{yx} mirrors M—AHE is mainly responsible for ρ_{yx}. The linear ρ_{yx} response at low magnetic fields and virtually closed hysteresis loops reflect the magnetization vector rotation from the in-plane easy axis to out-of-plane hard axis (Fig. S3 in the Supplementary Information). The wide-range linearity up to about $\pm 0.5\,\text{T}$ is beneficial for AHE-type Hall sensors.

The x dependence of saturation ρ_{yx} differs from that of the saturation M (Fig. 2a). To get insights into these composition dependences, we performed control experiments using high-temperature grown polycrystalline Fe_xSn_{1-x} films ($T_g = 500\,°\text{C}$), shown in Fig. 2c,d. In the polycrystalline films with $x = 0.62$ and 0.78, the overall anomalous Hall responses and saturation magnetic fields are similar to those of the nanocrystalline ones. In contrast, AHE and M are considerably small for $x = 0.54$ in which antiferromagnetic FeSn is dominant as revealed by XRD. In Fig. 2e, these x-dependent AHE properties are summarized using tangent of Hall angle, ρ_{yx}/ρ_{xx} (ρ_{xx}: longitudinal resistivity). As a consequence of a sharp ρ_{yx} peak around $x = 0.60$ and ρ_{xx} slightly changing with x (Fig. 2e inset), ρ_{yx}/ρ_{xx} takes a broad maximum around $x = 0.60$–0.75 in the nanocrystalline films. A weaker but
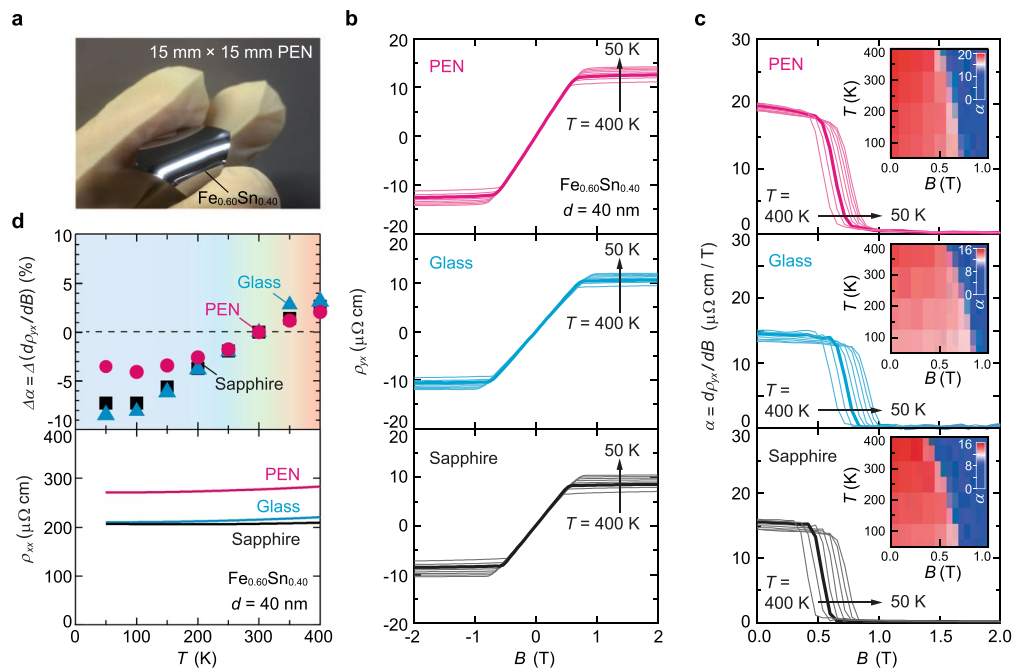
Figure 3. AHE on various substrates. (**a**) Photograph of a 40-nm-thick nanocrystalline $Fe_{0.60}Sn_{0.40}$ film on a flexible PEN sheet substrate. (**b**) ρ_{yx} of 40-nm-thick nanocrystalline $Fe_{0.60}Sn_{0.40}$ films on PEN sheet (magenta), glass (cyan), and sapphire (black) substrates. The AHE measurement was performed at $T = 50, 100, 150, 200, 250, 300, 350,$ and $400\,K$. The data at $300\,K$ are highlighted with bold lines. (**c**) Differential coefficient $\alpha = d\rho_{yx}/dB$. The insets display contour plots of α against T and B. (**d**) The T variation of α defined as $\Delta\alpha = (\alpha(T) - \alpha(T = 300\,K))/\alpha(T = 300\,K)$ and ρ_{xx} are shown in the upper and lower panels, respectively.

similar trend is also seen for the polycrystalline films that partly contain FeSn, Fe_3Sn_2, and Fe_3Sn (Fig. 1d). Note that such a composition dependence is not expected for mere Sn-rich α-Fe.

In Fig. 2f, T dependence of Hall conductivity $\sigma_{xy} = \rho_{yx}/(\rho_{xx}^2 + \rho_{yx}^2)$ is compared for nanocrystalline and polycrystalline films with $x \sim 0.6$ and also bulk Fe_3Sn_2 in literature[8]. The occurrence of nearly T-independent σ_{xy} in the polycrystalline films, which resembles the intrinsic behavior in Fe_3Sn_2 single crystals[8,13], but with a much smaller σ_{xy} than the bulk value suggests a small fraction of Fe_3Sn_2 domains crystalized by high-temperature sputtering ($T_g = 500\,°C$). Antiferromagnetic FeSn that persistently exists in the polycrystalline film, as found in the decreased M and ρ_{yx} (Fig. 2b,d, and also see Fig. S4 in the Supplementary Information), does not give positive contributions to the AHE. In stark contrast, σ_{xy} in the nanocrystalline film rivals the bulk data in the entire T range. One obvious reason for this is the suppression of FeSn by room-temperature sputtering. Although it is not clear whether the mechanism of the large AHE discussed for Fe_3Sn_2 single crystals (ref.[8]) is valid for such nanocrystalline Fe-Sn films, these observations demonstrate that the AHE in the Fe-Sn alloy system is maximized at specific compositions. The large ρ_{yx} and ρ_{yx}/ρ_{xx} observed for $x = 0.77$ may suggest that ferromagnetic Fe_3Sn (refs[24,25]) is also a large AHE material, though the transport properties have not been clarified yet.

Thermal stability of the AHE in room-temperature deposited films. Having confirmed the large AHE in the nanocrystalline Fe_xSn_{1-x}, we now turn to the characterization as a magnetic sensor element. Taking advantages of room-temperature sputtering, we extend our investigation to more commercially available substrates, glass and flexible polyethylene naphthalate (PEN) sheet (Fig. 3a, also see Fig. 1e for their XRD patterns). T-dependent AHE characteristics of $Fe_{0.60}Sn_{0.40}$ films with thicknesses $d \sim 40\,nm$, displayed in Fig. 3b, are essentially similar on the three substrates, demonstrating that specific substrates are not required to achieve the large AHE. Magnetic-field sensing can be performed in the almost linear $\rho_{yx} - B$ region, and the differential coefficient, $\alpha = d\rho_{yx}/dB$, corresponds to the sensitivity for B via V_{yx}. As displayed in Fig. 3c and inset, α is nearly constant to a large B of approximately $0.5\,T$, and is rather insensitive to the T variation (red colored regions in the inset). This is more clearly seen in the upper panel of Fig. 3d, where the temperature stability of α is tracked, defined as $\Delta\alpha = (\alpha(T) - \alpha(T = 300\,K))/\alpha(T = 300\,K)$. In a general operation range of $T = 200-400\,K$, $\Delta\alpha$ is within a few percent, corresponding to approximately $0.02\%/K$. The small variation in ρ_{xx}, shown in the lower panel, gives an advantage over semiconductor devices that are restricted by inherent thermally activated transport[26].

Characterization of Hall sensor responses and flexibility. To enhance V_{yx} further in view of the film thickness d ($V_{yx} = I \times \rho_{yx}/d$), we examined the lower bound of d. Judging from the d dependences of ρ_{xx}, ρ_{yx}, and ρ_{yx}/ρ_{xx} at $B = 2\,T$ (Fig. 4a) and also V_{yx} versus B curves (Fig. 4b), we determine that the applicable large AHE persists down to $d = 4\,nm$. The d decrease to $2\,nm$ is possible for ρ_{yx}, but is accompanied by a sharp rise in ρ_{xx} and the drop of ρ_{yx}/ρ_{xx}. These increase power consumption when supplying a constant excitation current (I). In other
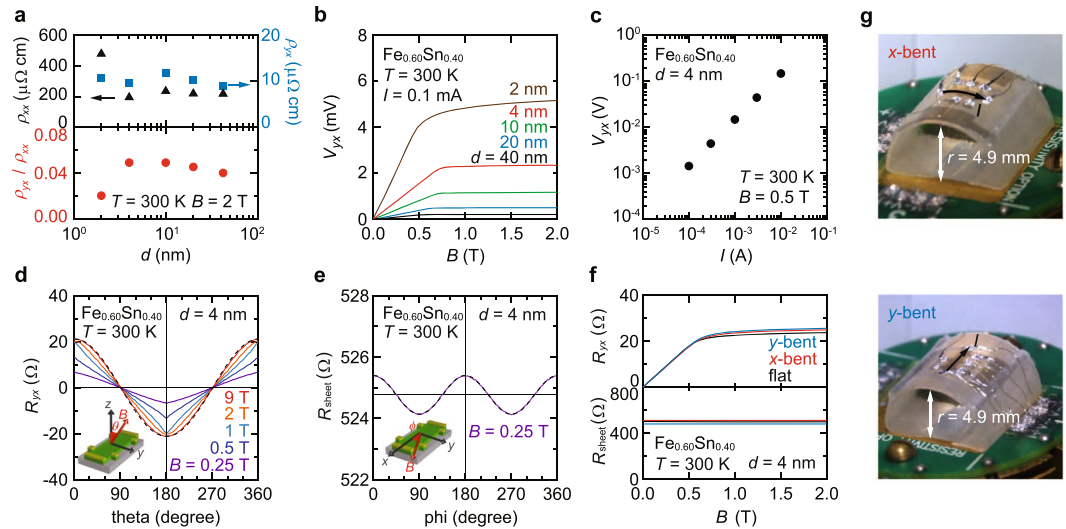
Figure 4. Magnetic sensor properties of nanocrystalline $Fe_{0.60}Sn_{0.40}$ films. (**a**) Thickness (d) dependences of ρ_{xx}, ρ_{yx} and ρ_{yx}/ρ_{xx} measured for a nanocrystalline $Fe_{0.60}Sn_{0.40}$ film on sapphire (0001) at $B = 2\,T$. (**b**) V_{yx} versus B curves measured at $I = 0.1\,mA$ for $d = 40\,nm$ (black), $20\,nm$ (blue), $10\,nm$ (green), $4\,nm$ (red), and $2\,nm$ (brown). (**c**) V_{yx} output characteristics as a function of I. (**d**) Out-of-plane magnetic field angle (θ) dependence of R_{yx} for a 4-nm-thick nanocrystalline $Fe_{0.60}Sn_{0.40}$ film on sapphire (0001). The measurement setup is shown schematically in the inset. The black dotted curve represents a relation $R_{yx} \propto \cos\theta$. (**e**) Anisotropic magnetoresistance measurement. Sheet resistance R_{sheet} was measured in an in-plane B. The in-plane rotation angle (ϕ) is defined in the inset. The dotted curve is a fitting result using a $\cos 2\phi$ function. (**f**) Bending effects on transport properties of a 4-nm-thick $Fe_{0.60}Sn_{0.40}$ film on PEN. See Fig. 4g for the definition of x-bent and y-bent. The sample was first measured without bending (flat, black curves), and subsequently characterized under x-bent (red) and y-bent (blue) conditions. After these cycles, the device recovered back to the initial flat state (Fig. S5). (**g**) Photographs of the x-bent and y-bent devices. 4-nm-thick films on PEN sheet substrates were mounted on the surface of a 4.9-mm-radius semicircular jig in two different geometries.

words, at the fixed input voltage, V_{yx} is reduced by the decreased I. The 1-nm-thick device was no longer conductive; d of approximately 2 nm may be the critical thickness where island-like domains start to coalesce and form conduction paths. As presented in Fig. 4c, by injecting $I = 10\,mA$ into the 4-nm-thick device, a large V_{yx} exceeding 0.1 V is generated from a magnetic field of $B = 0.5\,T$.

We would like to here note some specific features, which are potentially utilized for three-dimensional magnetic-field sensing. Figure 4d shows out-of-plane magnetic field angle dependences of R_{yx} under various B, measured for the 4-nm-thick $Fe_{0.60}Sn_{0.40}$ film on sapphire (0001) (the inset: the schematic measurement configuration). At $B = 9\,T$, R_{yx} obeys a $\cos\theta$ relation (black dotted curve) as expected from $M_{eff} \propto B_{eff} = B\cos\theta$ with M_{eff} and B_{eff} being the out-of-plane components of magnetization and magnetic field, respectively. As B is decreased, because of the in-plane magnetic easy axis (see Fig. S3 in the Supplementary information), the actual direction of M vector becomes not to fully follow that of B vector, resulting in a deviation from the $\cos\theta$ relation. Also, the in-plane magnetoresistance R_{sheet} vs ϕ, shown in Fig. 4e, indicates an anisotropic magnetoresistance effect even at low $B = 0.25\,T$ (the inset: the schematic measurement configuration). By combining these anisotropic responses of R_{yx} and R_{sheet}, the magnetic field vector $B(\theta, \phi)$ could be detected with a simple Hall-bar device.

Nanocrystalline Fe_xSn_{1-x} as demonstrated above can be served as a Hall-type magnetic sensor. In particular, the capability of sensor integration onto a flexible substrate is appealing, potentially finding applications in flexible electronics[27]. We examined the mechanical bending effect on a nanocrystalline Fe_xSn_{1-x} device using flexible PEN substrates. Figure 4f demonstrates that, even under severe bending conditions (see Fig. 4g for the definition of bending geometries), the nanocrystalline $Fe_{0.60}Sn_{0.40}$ device on PEN offers a reversible operation with an almost unchanged sensor performance (Fig. S5 in the Supplementary Information). Such new functionality enabled by nanocrystalline Fe_xSn_{1-x} films, in combination with its economically and environmentally friendly ingredients, would offer a new type of magnetic sensor design utilizing AHE.

Discussion and Conclusions

Large ρ_{yx} at room temperature has also been obtained in ferromagnetic semiconductors[28] and metal-insulator composites[29]. According to the established classification of AHE origins[11,30,31], those highly resistive materials, however, are in the poorly conductive region ($\sigma_{xx} < \sim 3 \times 10^3\ \Omega^{-1}\,cm^{-1}$). Our nanocrystalline Fe_xSn_{1-x} is essentially a metal with σ_{xx} as high as mid - 10^3–$10^4\ \Omega^{-1}\,cm^{-1}$, being in a different category called the intrinsic region (Fig. S6 in the Supplementary Information). In fact, it is observed in nanocrystalline Fe_xSn_{1-x} films that σ_{xy} is rather independent of σ_{xx}, as being consistent with intrinsic mechanisms. At present, the sensitivity of our device is about one order of magnitude lower than those of the state-of-the-art GaAs and Si Hall sensors[32]. If the Berry curvature mechanism[8] holds for the AHE in nanocrystalline Fe_xSn_{1-x} films, the device performance could be further improved by Fermi-level tuning into the gap at the Dirac point[8]. Such an intrinsic approach, in addition

5

to its critical importance for the next-generation of Hall sensors, may also lead to devices that incorporate exotic quantum transport phenomena, e.g., quantized AHE. We believe that the thin-film structure would be the key enabler for exploration of new functionality that emerges on the kagome lattice.

Methods

Thin-film growth. Fe_xSn_{1-x} alloy films were fabricated by RF magnetron sputtering. The RF power was 50 W, and Ar gas pressure was 0.5 Pa for $x < 0.87$ and 0.8 Pa for $x = 0.87$. The typical growth rate was approximately 4 nm/min as checked by X-ray reflectivity measurement and also with a surface profiler. For films with $d \leq 4$ nm, the surface was covered with a 15-nm-thick SiO_x insulating layer to prevent oxidation. The SiO_x layer was formed by RF magnetron sputtering using a SiO_2 target at an Ar gas pressure of 0.5 Pa. Compositional analysis of the films was performed with energy-dispersive X-ray spectroscopy and inductively coupled plasma atomic emission spectroscopy.

AHE and magnetization measurements. Electrical transport properties were measured with a VersaLab, a Physical Property Measurement System (Quantum Design) and a source-measure unit. Films were patterned into a Hall-bar structure (1b), and electrical contacts were made with an indium solder. The aspect ratio of electrode-electrode distance for V_{xx} versus that for V_{yx} was approximately unity. To remove thermoelectric and geometric effects, the measured data were symmetrized for V_{xx} and anti-symmetrized for V_{yx} against B as widely adopted to these measurements. Magnetization measurements were carried out using a vibrating sample magnetometry mode of VersaLab.

References

1. Coey, J. M. D. Permanent magnet applications. *J. Magn. Magn. Mater.* **248**, 441–456 (2002).
2. Sugimoto, M. The past, present, and future of ferrites. *J. Am. Ceram. Soc.* **82**, 269–280 (1990).
3. Weiss, R. J. The origin of the 'Invar' effect. *Proc. Phys. Soc.* **82**, 281 (1963).
4. Wolf, S. A. *et al.* Spintronics: a spin-based electronics vision for the Future. *Science* **264**, 1488–1495 (2001).
5. Takanashi, K., Mizuguchi, M., Kojima, T. & Tashiro, T. Fabrication and characterization of $L1_0$-ordered FeNi thin films. *J. Phys. D.: Appl. Phys.* **50**, 483002 (2017).
6. Laurent, S. *et al.* Magnetic iron oxide nanoparticles: synthesis, stabilization, vectorization, physicochemical characterizations, and biological applications. *Chem. Rev.* **108**, 2064–2110 (2008).
7. Bhattacharyya, S. Iron nitride family at reduced dimensions: a review of their synthesis protocols and structural and magnetic properties. *J. Phys. Chem. C* **119**, 1601–1622 (2015).
8. Ye, L. *et al.* Massive Dirac fermions in a ferromagnetic kagome metal. *Nature* **555**, 638–642 (2018).
9. Lenz, J. & Edelstein, A. S. Magnetic sensors and their applications. *IEEE Sensors J.* **6**, 631–649 (2006).
10. Heremans, J. Solid-state magnetic field sensors and applications. *J. Phys. D* **26**, 1149–1168 (1993).
11. Nagaosa, N., Sinova, J., Onoda, S., MacDonald, A. H. & Ong, N. P. Anomalous Hall effect. *Rev. Mod. Phys.* **82**, 1539–1592 (2010).
12. Kida, T. *et al.* The giant anomalous Hall effect in the ferromagnet Fe_3Sn_2—a frustrated kagome metal. *J. Phys.: Condens. Matter* **23**, 112205 (2011).
13. Wang, Q., Sun, S., Zhang, X., Pang, F. & Lei, H. Anomalous Hall effect in a ferromagnetic Fe_3Sn_2 single crystal with a geometrically frustrated Fe bilayer kagome lattice. *Phys. Rev. B* **94**, 075135 (2016).
14. Haldane, F. D. M. Model for Quantum Hall effect without Landau levels: condensed-matter realization of the "parity anomaly". *Phys. Rev. Lett.* **61**, 2015–2018 (1988).
15. Chang., C.-Z. *et al.* Experimental observation of the quantum anomalous Hall effect in a magnetic topological insulator. *Science* **340**, 167–170 (2013).
16. Giefers, H. & Nicol, M. High pressure X-ray diffraction study of all Fe-Sn intermetallic compounds and one Fe-Sn solid solution. *J. Alloys Compd.* **422**, 132–144 (2006).
17. Fenner, L. A., Dee, A. A. & Wills, A. S. Non-collinearity and spin frustration in the itinerant kagome ferromagnet Fe_3Sn_2. *J. Phys.: Condens. Matter* **21**, 452202 (2009).
18. Haftek, E., Tan, M. & Barnard, J. A. Microstructure and magnetic properties of ferromagnetic Fe-Sn alloy thin films. *Ultramicroscopy* **47**, 400–407 (1992).
19. Gao, J. *et al.* Giant Hall effect in Fe_xSn_{100-x} granular alloy films. *J. Appl. Phys.* **93**, 1851 (2003).
20. Nakatsuji, S., Kiyohara, N. & Higo, T. Large anomalous Hall effect in the colinear antiferromagnet at room temperature. *Nature* **527**, 212–215 (2015).
21. Kuroda, K. *et al.* Evidence for magnetic Weyl fermions in a correlated metal. *Nat. Mater.* **16**, 1090–1095 (2017).
22. Nayak, A. K. *et al.* Large anomalous Hall effect driven by a nonvanishing Berry curvature in the noncolinear antiferromagnet Mn_3Ge. *Sci. Adv.* **2**, e1501870 (2016).
23. Liu, E. *et al.* Giant anomalous Hall effect in a ferromagnetic kagome-lattice semimetal. *Nat. Phys.* **14**, 1125–1131 (2018).
24. Trumpy, G., Both, E., Djega-Mariadassou, C. & Lecocq, P. Mössbauer-Effect studies of Fe-Sn Alloys. *Phys. Rev. B.* **2**, 3477–3490 (1970).
25. Sales, B. C., Saparav, B., McGuire, M. A., Singh, D. J. & Parker, D. S. Ferromagnetism of Fe_3Sn and alloys. *Sci. Rep.* **4**, 7024 (2014).
26. Jankowski, J., El-Ahmar, S. & Oszwaldowski, M. Hall sensors for extreme temperatures. *Sensors* **11**, 876–885 (2011).
27. Ohta, S., Ando, A. & Chiba, D. A flexible giant magnetoresistive device for sensing strain direction. *Nat. Electron.* **1**, 124–129 (2018).
28. Tu, N. T., Hai, P. N. & Tanaka, M. High-temperature ferromagnetism in heavily Fe-doped ferromagnetic semiconductor (Ga,Fe)Sb. *Appl. Phys. Lett.* **108**, 192401 (2016).
29. Sonntag, J. The Origin of the Giant Hall Effect in Metal-Insulator Composites. *Open Journal of Composite Materials* **5**, 78–90 (2016).
30. Onoda, S., Sugimoto, N. & Nagaosa, N. Intrinsic versus extrinsic anomalous Hall effect in ferromagnets. *Phys. Rev. Lett.* **97**, 126602 (2006).
31. Fukumura, T. *et al.* A scaling relation of anomalous Hall effect in ferromagnetic semiconductors and metals. *Jpn. J. Appl. Phys.* **46**, L642 (2007).
32. Ripka, P. & Janosek, M. Advances in magnetic field sensors. *IEEE Sensors Journal* **10**, 1108 (2010).

Acknowledgements

Author Contributions

Additional Information

Supplementary information accompanies this paper at https://doi.org/10.1038/s41598-019-39817-8.

Competing Interests: The authors declare no competing interests.

Publisher's note: Springer Nature remains neutral with regard to jurisdictional claims in published maps and institutional affiliations.